Journal of Applied Physics

Perspective: Principles and specifications of photothermal imaging methodologies and their applications to non-invasive biomedical and non-destructive materials imaging

Cite as: J. Appl. Phys. **124**, 160903 (2018); https://doi.org/10.1063/1.5044748
Submitted: 15 June 2018 . Accepted: 13 October 2018 . Published Online: 29 October 2018

Pantea Tavakolian, and Andreas Mandelis

AIP Publishing

Perspective: Principles and specifications of photothermal imaging methodologies and their applications to non-invasive biomedical and non-destructive materials imaging

Pantea Tavakolian[1] and Andreas Mandelis[1,2,a)]
[1]*Center for Advanced Diffusion-Wave and Photoacoustic Technologies (CADIPT), Department of Mechanical and Industrial Engineering, University of Toronto, Toronto, Ontario M5S3G8, Canada*
[2]*Institute of Biomaterials and Biomedical Engineering, University of Toronto, Toronto, Ontario M5S 3G9, Canada*

(Received 15 June 2018; accepted 13 October 2018; published online 29 October 2018)

This article discusses a number of dynamic thermography techniques used for analysis of captured raw infrared images of objects. The most widely used, as well as state-of-the-art, modalities are outlined in terms of their operating principles and their specifications. Special attention is paid to truncated correlation photothermal coherence tomography, a novel method that provides high contrast and high resolution 3D images of objects. Applications of thermography in medical imaging, art analysis, and non-destructive imaging of industrial materials are discussed. *Published by AIP Publishing.* https://doi.org/10.1063/1.5044748

I. INTRODUCTION

Thermography is a technique whereby the condition of objects is studied by means of precisely monitoring temperature variations over the surface of such objects. In the past few decades, there has been increased interest in active infrared thermography for non-destructive imaging (NDI) of industrial materials and art objects and medical diagnosis applications. Industrially, thermography is used in military, aerospace, power generation, and automotive industry applications to detect both manufacturing and in-service environment-induced defects.[1–8] Recently, research was undertaken to apply thermal imaging in the field of art conservation to examine structures of panel paintings, marquetries, and other art objects for diagnostics and authentication purposes.[9–12] Thermography is a non-contact, non-ionizing, fast, and reliable technique and is receiving growing attention in the medical field. This technique is utilized in the detection of early caries in teeth with better sensitivity than radiography[13–16] and bone imaging with the aim of establishing a diagnostic technique for osteoporosis.[17,18] In breast thermal imaging, an abnormal infrared image has been proven to be an effective marker for a high risk of developing breast cancer.[19–22]

Dynamic thermography based on several signal processing methods has been proposed to improve the performance of photothermal systems being either in the time domain or in the frequency domain. For the time-domain techniques, the resulting amplitude images are very prone to local optical and infrared surface features such as non-uniform heating, emissivity variation, ambient reflections, and sample surface conditions.[23] However, frequency domain techniques give rise to phase images and carry more information about the sample. Phase images are emissivity normalized and thus superior to amplitude images in terms of depth probing capability as they probe deeper than amplitude.[23–26] Lock-in thermography (LIT), a well-known infrared imaging modality, determines the amplitude and phase of the sample temperature oscillations ("thermal waves").[27] Since LIT rejects noise signals at frequencies other than the reference frequency, it provides high signal-to-noise ratio (SNR) thermal wave images. In 1996, lock-in reconstruction algorithms combined with pulsed photothermal radiometry (PPTR)[28–31] provided faster and higher penetration depth and resolution thermal images than conventional dc infrared thermography. In this technique, phasograms (phase maps) are of particular interest, and for this reason the modality is called pulsed phase thermography (PPT).[32]

Many attempts have been made to localize energy in the thermal-wave field and to overcome the axial resolution limitations imposed by the parabolic diffusion waves. Thermal waves are governed by the parabolic heat diffusion equation and therefore lack wave fronts causing depth-integrated (rather than localized) energy distribution. The diffuse nature of heat conduction in a medium results in poor axial resolution, which degrades with time and distance from the source. Historically, the first signal processing method proposed in the heat conduction field to improve the axial resolution was pseudorandom binary sequence (PRBS) optical excitation followed by match-filtering.[33] Later on, frequency modulated photothermal wave spectroscopy was proven to provide accurate determination of the system impulse response function, superior dynamic range properties, and a faster response compared to PRBS excitation.[34–36] More recently, the concept of cross-correlation match-filtering was used for localizing energy of the received signal under a single peak located at a delay time τ_p equal to the delay time between transmitted and received signals.[37,38] More energy localization was achieved by incorporating a pulse compression methodology which reduces the cross-correlation width while increasing its peak height. Linear frequency modulation (LFM) excitation (wide-band frequency modulation)[38] or

a)mandelis@mie.utoronto.ca. Telephone: +01-416-978-5106.

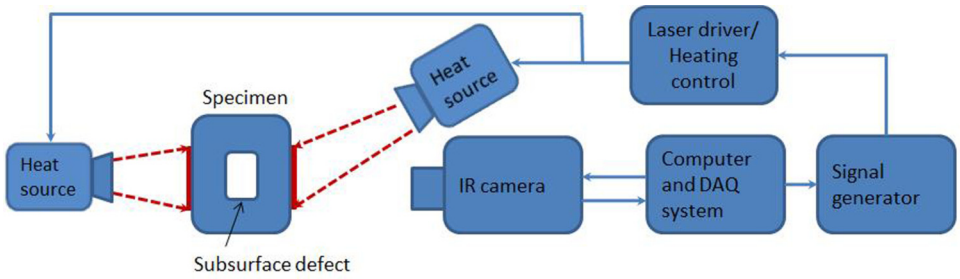

FIG. 1. Active thermography system.

Binary Phase Coded (BPC) modulation (narrow-band phase encoding)[39] are two kinds of pulse compression techniques. Incorporation of the cross-correlation technique with LFM excitation and with BPC beam modulation introduced the concept of thermal wave radar (TWR) and thermal coherence tomography (TCT), respectively. Subsequently, chirp pulsed excitation signals (with constant pulse-width) were combined with the TWR reconstruction algorithm and exhibited SNR improvement up to two orders of magnitude compared to three distinct chirped excitation waveforms (sine-wave, square-wave, and constant duty cycle pulses) under equal exposure energy of lower than 100 mJ.[17]

Recently, truncated correlation photothermal coherence tomography (TC-PCT) was introduced[40] and later enhanced,[26] thus becoming the only dynamic thermal imaging method that provides a highly axially resolved 3D image of a specimen. Apart from chirped pulse excitation with fixed pulse width and pulse-compression, TC-PCT uses a time-evolving filter to reconstruct the depth distribution of photothermal parameters and provides 2D and 3D images of a sample as the photothermal analog of optical coherence tomography (OCT).

Among the main kinds of frequency domain active thermography are lock-in thermography (LIT), pulse phase thermography (PPT), thermal wave radar (TWR), binary phase coding thermal coherence tomography (BPC-TCT), chirp pulse photothermal radar (CPPTR), and truncated correlation photothermal coherence tomography (TC-PCT). Here, we review these data analysis methodologies and their applications, specifications, advantages, and disadvantages.

II. THERMAL IMAGING INSTRUMENTATION AND SIGNAL GENERATION

A generic active thermography instrumentation scheme includes a light source (a broadband lamp, flash controls, heat gun, or a diode laser followed by a beam homogenizer),[41] a single detector or an IR camera (usually in the spectral range of 1–5 μm) that measures surface temperature, signal generator triggered by a computer, data acquisition system, and a computer to synchronize the systems and to perform signal processing on the raw infrared images (Fig. 1). Both transmission[42,43] and backscattering[44] modes can be employed to perform thermography, but the backscattering mode is more attractive as it is not always possible to have access to the other side of the object. The procedure to perform thermography can be divided into 4 steps depicted in Fig. 1. First, the specimen's surface is heated with a thermal source (e.g., using photographic flashes in PPT or using a laser acting as a photothermal heat source in TC-PCT. All reported images in this report were generated with 808 nm diode laser excitation). A heating controller (e.g., laser driver) is usually needed to drive the heating source and to modulate the beam. The controller is connected to a signal generator to receive the modulating signal. Second, the thermal signal continues to diffuse through the material bulk following the heat deposition cutoff at the surface. Third, the surface temperature conductive change is monitored using an infrared camera. A thermal map of the surface is recorded at constant time intervals creating a video of the temperature evolution. Finally, in the fourth step, the thermogram sequence is processed with the reconstruction algorithm on a computer. Sometimes, a data acquisition system is needed to record the modulating optical signal that heats the sample surface for post-processing algorithms. Studying different reconstruction algorithms is the focus of this paper.

In photothermal imaging techniques, the illumination schemes can be either continuous wave (CW) or pulsed excitation. In the CW method, the excitation signal is in the form of a low-power, continuous, amplitude/frequency modulated pattern. The sample thermal response to harmonic stimulation is described by an oscillating thermal wave. In the pulsed thermography (PT) method, however, a few-millisecond high-power optical pulse impinges on a material and the following temperature decay are recorded. An ideal Dirac pulse $\delta(t)$ in the time domain has an infinite flat spectrum in the frequency domain. When a specimen is pulse heated, a rectangular pulse instead of the ideal Dirac pulse is used; thus, thermal waves of many frequencies with various amplitudes instead of a constant amplitude are simultaneously launched into the sample. For a rectangular pulse of width τ and amplitude A centered at $t = 0$, the frequency content is expressed by the well-known sinc waveform, $A\tau\sin(\omega\tau)/\omega\tau$, where ω is the angular frequency. Therefore, unlike CW, PT generates a broad spectrum of frequencies in a specimen.

Depending on the incident radiation, an oscillatory or a transient thermal wave is generated in the sample. Analytically, photothermal heat diffusion models can be developed in a sample by solving a heat conduction boundary value problem. To date, solutions to the heat diffusion problem for different excitation signals and a wide range of geometries and materials have been derived.[45–48] In all the solutions, thermal diffusion length ($\mu = \sqrt{2\alpha/\omega}$), and heat transfer rate ($\nu = \sqrt{2\alpha\omega}$) play key roles as they indicate penetration depth and propagation speed in a sample with a thermal diffusivity α, at a specific modulation frequency $f = \frac{\omega}{2\pi}$. Thermal diffusion length is inversely proportional to

the square root of modulation frequency, while propagation speed is proportional to the square root of frequency. These facts indicate that high frequency thermal waves limit their diffusion close to the surface, while low frequency heat waves dissipate to a deeper region, but slowly.

III. DATA ANALYSIS METHODOLOGIES

A. Lock in thermography (LIT)

LIT has been applied to infrared data to enhance the SNR of thermal images.[13,38,40,49] Typically, a sample is excited at a fixed frequency and the LIT method records the demodulated output signal at this reference frequency. Suppose the excitation signal is a *sine* wave at angular frequency ω with a large heating beam radius to satisfy one dimensional heat flow. When the heating source is localized on the surface of an object as a result of light absorption, the conductive heat flow inside the material is given by Eq. (1).

$$\begin{aligned} S(z,t) &= \mathrm{A}(z)\cos\left[\omega t - \varphi(z)\right] \\ &= T_0 e^{-z/\mu}\cos\left(\omega t - \frac{z}{\mu} - \varphi_I\right). \end{aligned} \tag{1}$$

The thermal-wave response recorded by a single detector or a camera will be proportional to $S(0,t) = T_0\cos(\omega t - \varphi_I)$ where T_0 is the initial change in the temperature (signal amplitude), ω is the modulation angular frequency, μ is the thermal diffusion length, and $\varphi(z)$ and φ_I are the phases at depth z and the initial phase, respectively.[50] The lock-in technique multiplies the response signal by the reference signal, $T_R\cos(\omega t + \varphi_R)$, and filters the output with a low pass filter.

$$\begin{aligned} S_{m1} &= T_0\cos(\omega t - \varphi_I)\times T_R\cos(\omega t - \varphi_R) \\ &= \frac{1}{2}T_0T_R\cos(\varphi_R - \varphi_I) + \frac{1}{2}T_0T_R\cos(2\omega_R t - \varphi_R - \varphi_I), \end{aligned} \tag{2}$$

$$S_{m1-filtered} = \frac{1}{2}T_0T_R\cos(\varphi_R - \varphi_I). \tag{3}$$

The filtered output is proportional to the cosine of the phase difference between the input and the reference signals. To measure the thermal-wave amplitude and phase, the reference signal 90° out of phase is also multiplied with the response signal [Eq. (4)] and low pass filtered [Eq. (5)]. Then, amplitude and phase are measured by Eqs. (6) and (7), respectively.

$$\begin{aligned} S_{m2} &= T_0\cos(\omega t - \varphi_I)\times T_R\cos\left(\omega t - \varphi_R - \frac{\pi}{2}\right) \\ &= \frac{1}{2}T_0T_R\cos\left(\varphi_R - \varphi_I + \frac{\pi}{2}\right) \\ &\quad + \frac{1}{2}T_0T_R\cos\left(2\omega_R t - \varphi_R - \varphi_I - \frac{\pi}{2}\right), \end{aligned} \tag{4}$$

$$\begin{aligned} S_{m2-filtered} &= \frac{1}{2}T_0T_R\cos\left(\varphi_R - \varphi_I + \frac{\pi}{2}\right) \\ &= \frac{1}{2}T_0T_R\sin(\varphi_R - \varphi_I), \end{aligned} \tag{5}$$

$$\begin{aligned} \textit{Demodulated amplitude}: A &= \frac{2}{T_R} \\ &\times\sqrt{(S_{m1-filtered})^2 + (S_{m2-filtered})^2}, \end{aligned} \tag{6}$$

$$\begin{aligned} \textit{Demodulated phase}: &\varphi_R - \varphi_I \\ &= tan^{-1}(S_{m2-filtered}/S_{m1-filtered}). \end{aligned} \tag{7}$$

To probe deeper, a low-frequency excitation signal needs to be applied leading to a longer acquisition time to obtain a proper number of periods, since increasing the number of periods aids in reducing the noise level and improves image quality. Besides the required longer acquisition time, low frequency thermal waves lack the desired resolution. Therefore, one needs to consider a compromise between maximum detection depth and depth resolution.

Since LIT performs at a single frequency, the detector captures information from a single diffusion length. To reconstruct a 3D image of the sample, the imaging should be repeated at different frequencies, and the computation should be performed for each scanned frequency, which is time consuming, and the result has a poor axial resolution.

B. Pulsed phase thermography (PPT)

More than 20 years ago, pulsed phase thermography (PPT) was introduced which combines pulse heating and lock in thermography and uses the merits of both approaches.[32] PPT provides better defect shape resolution than LIT, with the advantage that several frequencies are available with a single experiment.[51–53] In PPT, a specimen surface is illuminated by a pulse, and the temperature evolution on the inspected surface is monitored by an IR camera recording a thermal map (thermogram) of the surface at regular time intervals Δt and creating a 3D matrix *of* $N_x \times N_y \times N_t$, where N_x and N_y are dimensions of a single thermographic frame in pixels and N_t is the number of frames collected [Fig. 2(a)]. One recorded thermal transient of a pixel is displayed in Fig. 2(b).

PPT extracts various frequencies of a generated thermal transient followed by an excitation pulse and links it to different depths in the specimen. In the PPT technique, a one-dimensional discrete Fourier transform (DFT) is used to extract different frequencies. The DFT on each pixel of the thermogram sequence can be written as follows:

$$F_n = \Delta t\sum_{k=0}^{N-1} T(k\Delta t)e^{-2\pi ikn/N} = Re_n + iIm_n, \tag{8}$$

where $T(k\Delta t)$ is the sampled temporal evolution of each pixel in the field of view extracted from the image sequence, i is the imaginary unit, *Re* and *Im* are, respectively, the real and imaginary parts of the transform, subscript n designates the frequency increment ($n = 0, 1, \ldots, N$), and N is the total number of frames in the sequence. After computing Re_n and Im_n, the amplitude (A_n) and phase (φ_n) are measured with the

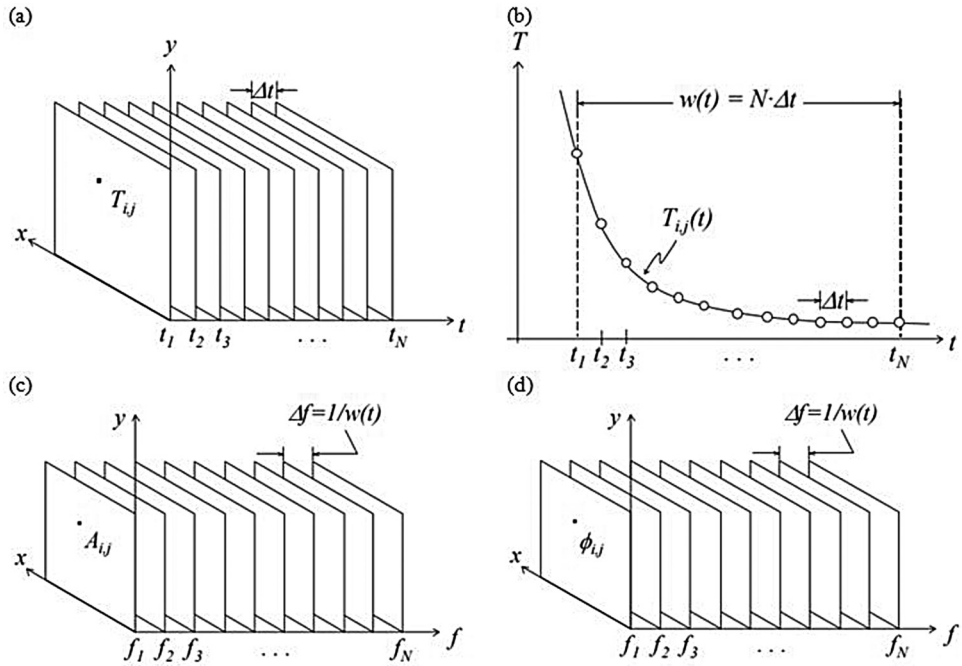

FIG. 2. Pulsed phase thermography algorithm. (a) Temperature 3D matrix in the time domain. (b) Temperature profile dependence of one pixel on coordinates (i,j). Frequency spectra amplitude (c) and phase matrices (d), calculated from Eq. (9).[52]

following formulas:

$$A_n = \sqrt{(Re_n^2 + Im_n^2)} \text{ and } \varphi_n = tan^{-1}\left(\frac{Im_n}{Re_n}\right). \quad (9)$$

The 3D matrix of recorded thermal signals is transformed to a 3D matrix in the frequency domain, and contrast (amplitude) profile and phase profile are measured from Eq. (9) [Figs. 2(c) and 2(d)].

Drawbacks of PPT are considerable noise content in phase data which increases with frequency[53] and limitation in quantitative analysis of the data. Therefore, different algorithms such as synthetic data[51] and the wavelet transform[54] are applied to the thermal signals for de-noising the phasograms and retrieving quantitative information from PPT results, respectively.

C. Thermal wave radar (TWR)

Despite the promising results of LIT, this modality cannot probe deeply into the sample as a result of reduced depth penetration of high-frequency thermal waves and reduced resolution of low-frequency thermal waves. Additionally, single frequency thermal waves yield depth integrated information from approximately a single diffusion length. Later, multi-frequency modalities were developed by Tabatabaei and Mandelis[38] and Mulaveesala *et al.*[37,55] as alternative solutions to this problem. The TWR uses a linear frequency modulation (LFM) pulse compression technique and cross-correlation signal processing.[34–36] In an LFM chirp as expressed in Eq. (10a), the instantaneous frequency changes linearly with time.

$$A(t) = A_0 \sin[2\pi f(t)t], \quad (10a)$$

$$f(t) = f_0 + kt, \quad (10b)$$

$$k = \frac{(f_e - f_s)}{2T}, \quad (10c)$$

where A_0, f_0, f_s, f_e, k, and T are the modulated waveform intensity, frequency modulation function, starting frequency, ending frequency, chirp sweep rate, and chirp time, respectively. This excitation waveform results in chirped thermal

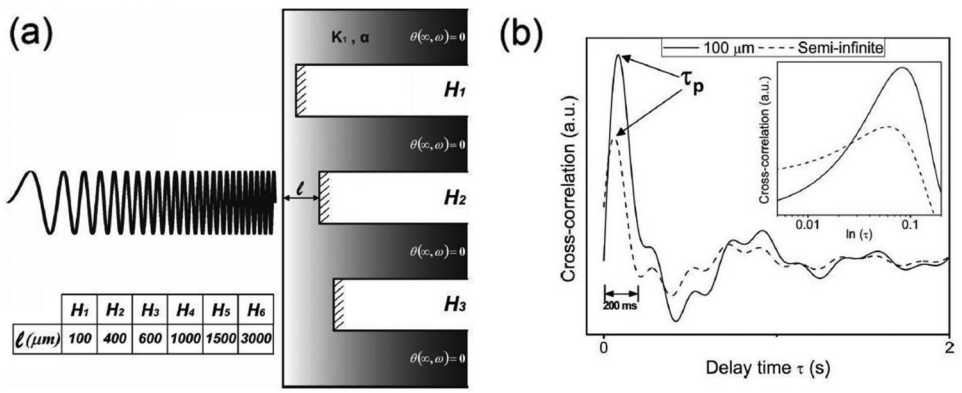

FIG. 3. TWR non-destructive testing of a steel sample. (a) A steel sample containing blind holes with steel overlayers of various thicknesses. (b) Theoretical TWR signals from a 100-μm thick and a semi-infinite steel sample. The inset magnifies the time interval of the main plot. As the steel sample thickness increases from 100 μm to infinity, the cross-correlation peak delay time decreases from 83 to 39 ms.[38,81]

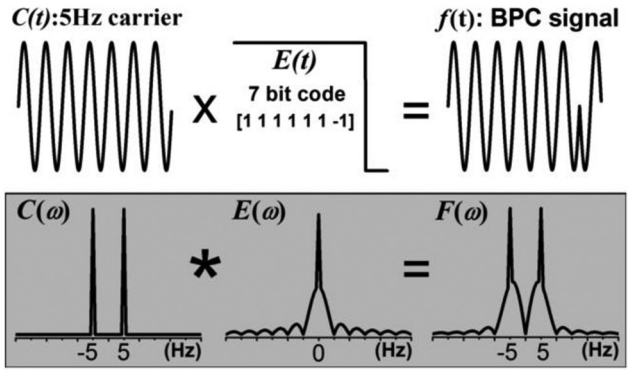

FIG. 4. Binary Phase Coding (BPC) signal construction in time (top) and frequency (bottom) domains for a 7-bit code and 5 Hz carrier.[57]

waves from the sample, yet embedded in noise. In the radar sciences, a match-filtering technique has been used to enhance range resolution and to improve SNR by detecting a pre-known signal within highly noised channels. The TWR method computes the cross-correlation between a reference waveform derived from the excitation waveform, $R(\tau)$, and the resulting photothermal signal, $S(t+\tau)$, measured at the delay time t, using the following equation:

$$C_R(t) = \int_{-\infty}^{\infty} R^*(\tau)S(t+\tau)d\tau. \tag{11}$$

Here $R^*(\tau)$ is the complex conjugate of the reference signal. Since the heat conduction process takes longer than the radiative (emissive) process to reach the surface, multiple sources at different depths can be detected as a result of cross-correlation with the reference pulse. The output of this cross-correlation contains a delayed peak, the delay being a function of thermophysical properties and the depth of sources below the specimen's surface. For example, for a steel sample with different subsurface hole thicknesses [Fig. 3(a)] the location of the TWR cross-correlation peak shifts toward shorter delay times as the depth increases [Fig. 3(b)]. This is due to the receding presence of the effective thermal source at the back interface as a result of coherent heat accumulation there.

D. Binary phase coding thermal coherence tomography (BPC-TCT)

Binary phase coding is another pulse compression technique that is widely used in radar sciences. While LFM excitation preserves a relatively constant power within the chirp frequency range, BPC modulation leads to a distinct energy localization advantage which is especially useful in diffusive fields. A comprehensive study on BPC can be found elsewhere.[39,56]

The BPC signal is formed by multiplying a single frequency carrier and a binary coded envelope in the time domain, or by convolving these two signals in the frequency domain [Fig. 4]. Then, the BPC signal excites the sample surface, and the stimulated thermal response gets recorded by the IR camera. Similar to TWR, the BPC-TCT images are constructed by first cross-correlating the photothermal signal and the excitation signal, and then by measuring the amplitude [Eq. (12)] and the phase [Eq. (13)] of the cross-correlation results.

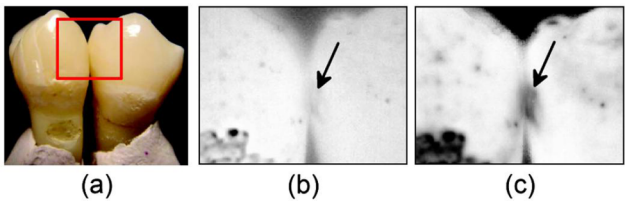

FIG. 5. Thermophotonic imaging of teeth. (a) Tooth matrix with hidden interproximal early caries. The red rectangle shows the imaged area. (b) Conventional LIT and (c) TCT phase images of the tooth matrix.[39]

$$A_{CC}(\tau) = \mathfrak{F}^{-1}[R(\omega)^* \times S(\omega)]\,, \tag{12}$$

$$\varphi_{cc}(\tau) = tan^{-1}\left(\frac{\mathfrak{F}^{-1}\{[-isgn(\omega)R(\omega)]^* \times S(\omega)\}}{\mathfrak{F}^{-1}[R(\omega)^* \times S(\omega)]}\right), \tag{13}$$

where $R(\omega)$ and $S(\omega)$ are the Fourier transforms of the reference/modulation signal, $R(t)$, and the photothermal signal, $s(t)$. $\mathfrak{F}^{-1}$, $*$, $sgn(\omega)$, and i denote the inverse Fourier transform, complex conjugation operator, signum function, and imaginary unit, respectively. Experimental results demonstrate that TCT imaging with the same modulation frequency and experimental conditions (averaging, laser power, etc.) maintains a better depth resolution than lock-in thermography.[39,57]

An example of TCT imaging of teeth matrix is provided in Fig. 5. The red rectangle shows the imaging area which covers a contacting surface between two teeth being demineralized to simulate early interproximal caries. LIT and TCT phase images [Figs. 5(b) and 5(c)] are formed under identical experimental conditions. TCT exhibits better axial resolution

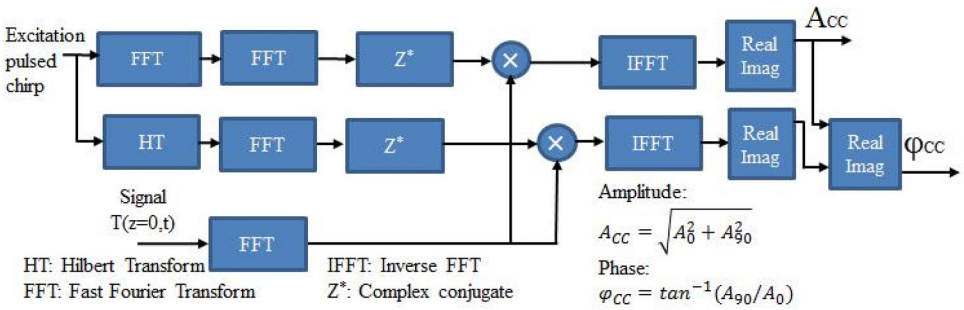

FIG. 6. CPPTR signal processing block diagram. A_{CC} and φ_{cc} are the amplitude and phase signals, respectively.[17,18]

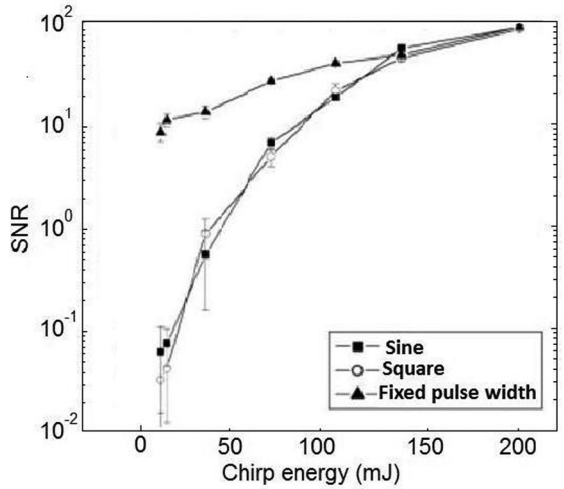

FIG. 7. SNR measurements for various chirp waveforms: sine, square, and fixed pulse-width chirps. Reprinted with permission from S. Kaiplavil and A. Mandelis, Rev. Sci. Instrum. **82**, 074906 (2011). Copyright 2011 AIP Publishing LLC.

over LIT, because matched-filter thermography yields higher localization of diffusive fields.

E. Chirped pulse photothermal radar (CPPTR)

CPPTR with superior depth probing over PPTR and an improved sensitivity over the harmonically modulated TWR combines pulsed chirp heating with the match-filtering technique.[17,18] The reconstruction scheme of CPPTR is shown in Fig. 6 which is similar to the match-filtering thermography techniques presented in Secs. III C and III D. The signal processing method cross-correlates the excitation signal and the response thermal transient in the frequency domain for fast computation. Then, amplitude and phase are calculated using Eqs. (12) and (13), respectively.

This method exhibits improved SNR by minimizing the static (dc) component of the photothermal signal and making use of the Planck radiation emission nonlinearity. The SNR of three excitation waveforms (sine-wave, square-wave, constant width pulses) chirping the pump laser under identical exposure energy for various chirp energies was measured.[18] The study proved that among the three distinct chirped excitation waveforms, constant-width pulse chirp with chirp energy lower than 100 mJ exhibits SNR improvement up to two orders of magnitude compared to all other equal energy modalities [Fig. 7].[17] The generated photothermal signal has dynamic (ac) and static temperature rise (dc background) components, the latter being cumulative in nature over several repetition cycles. Compared to CW excitation, pulsed signals minimize the static component of the photothermal signal resulting in greater SNR.

F. Truncated-correlation photothermal coherence tomography (TC-PCT)

Detection of depth-integrated distributions of energy is a shortcoming intrinsically characteristic of diffusion-wave fields. When 3D visualization of the sample is required, this is a serious limiting factor.[23] Truncated-correlation photothermal coherence tomography (TC-PCT),[40] and enhanced TC-PCT[26] as recently introduced, is the only dynamic thermal imaging modality to-date that provides axially resolved 3D images of materials and tissues.

The TC-PCT signal processing algorithm and examples of reference signals (R_n) and the thermal response signal (S) are shown in Figs. 8(a) and 8(b), respectively. In the TC-PCT technique, a generated LFM pulsed chirp excitation signal is employed to produce the in-phase reference signal (R_0) and its quadrature (R_{90}). First, the excitation waveform is passed through a square–wave chirp, and then a delay-incremented unit ($C_{1f,0}$). Next, the delay-incremented square-chirp is transmitted through a frequency doubler ($C_{2f,0}$), and the delay-incremented square-chirp ($C_{1f,0}$) and its doubled frequency waveform ($C_{2f,0}$) are subjected to the binary exclusive-OR (EX-OR) operation to produce a

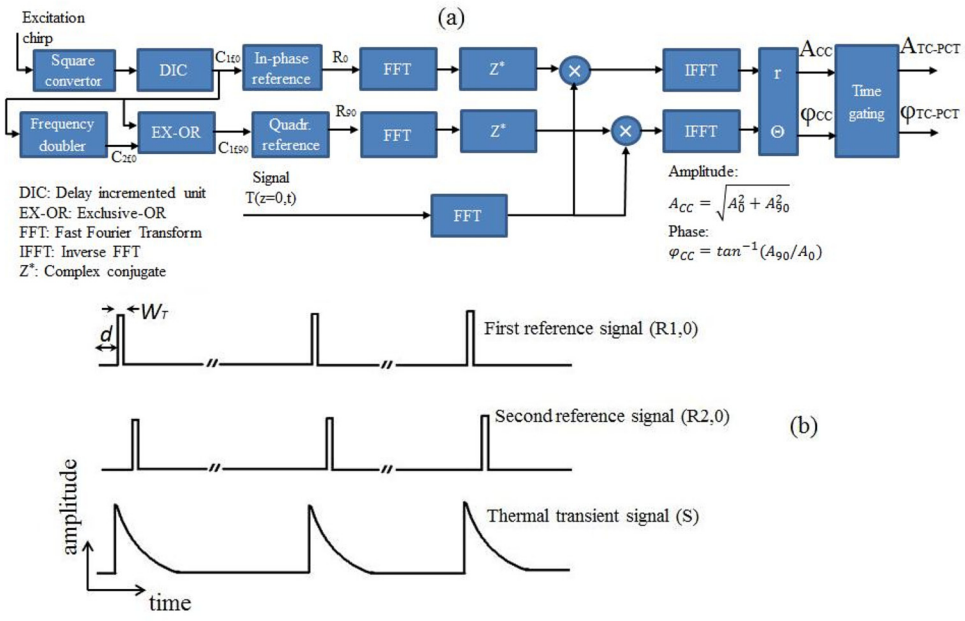

FIG. 8. Enhanced TC-PCT algorithm. (a) Enhanced TC-PCT reconstruction algorithm, and amplitude and phase measurements; (b) An example of the shape of the first and the second truncated reference pulses ($R_{1,0}$ and $R_{2,0}$), and the photothermal chirp signal (S). The time scales for reference signals are not the same as the thermal transient signal; they are exaggerated so as to show the duration of the optical pulse.[26]

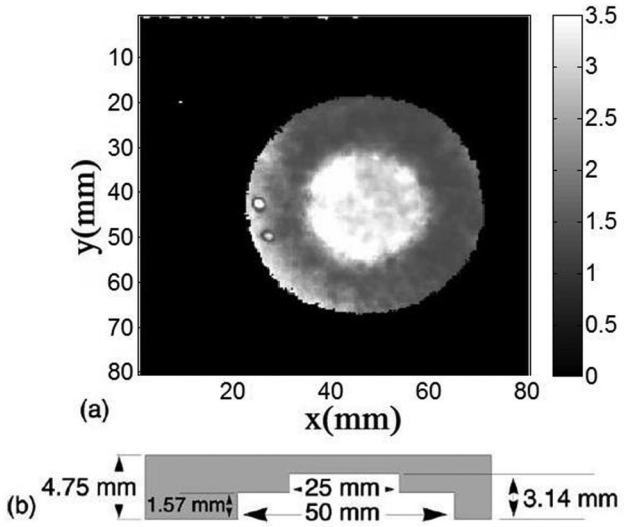

FIG. 9. Non-destructive defect detection in an aluminum sample using the PPT approach with the wavelet transform.[51] (a) Phase PPT image of the defects. (b) Aluminum sample geometry with two circular flat-bottom holes (one milled in the middle of the other).

quadrature square chirp. The reference signal R_0 and its quadrature R_{90} are then synthesized from $C_{1f,0}$ and $C_{1f,90}$, respectively. In contrast to CPPTR where the Hilbert transform is used to produce the quadrature of the chirp signal, TC-PCT uses the EX-OR operator to avoid generating spikes at the rising and falling edges of the rectangular pulses of the quadrature chirp waveform. In TC-PCT, similar to CCPTR and TWR, the reconstruction of the photothermal signals is based on the cross-correlation technique and is performed in the frequency domain for fast calculation. Then, the cross-correlation amplitude and phase are constructed from the expressions

$$A_{CC,n} = \sqrt{\{\mathfrak{F}^{-1}[R_n(\omega)^* \times S(\omega)]\}^2 + (\mathfrak{F}^{-1}\{[-isgn(\omega)R_n(\omega)]^* \times S(\omega)\})^2} \tag{14}$$

and

$$\varphi_{cc,n} = tan^{-1}\left(\frac{\mathfrak{F}^{-1}\{[-isgn(\omega)R_n(\omega)]^* \times S(\omega)\}}{\mathfrak{F}^{-1}[R_n(\omega)^* \times S(\omega)]}\right). \tag{15}$$

The time gating unit in the enhanced TC-PCT algorithm filters the cross-correlation amplitude and phase which is measured for every reference signal (R_n) and the photothermal response (S), with the following time gating width:

$$\textit{Time gating width} = \textit{Shortest pulse distance} - (n-1) \times d, \tag{16}$$

where "*the shortest pulse distance*" is the distance between the last two consecutive pulses in the full duration of the up-chirp excitation waveform, n is the TC-PCT slice number, and d is the constant delay applied to the reference signal by the delay incremented unit. Generally, the constant delay d has the same value as the slice width shown in Fig. 8(b) with the W_T label. Axial resolution in the 3D TC-PCT image of the sample depends on this slice width (W_T). To achieve high axial resolution, a small slice width should be selected which, however, localizes less energy within the slice thickness thus leading to lower TC-PCT signal quality. The minimum value for the W_T is limited by the camera frame

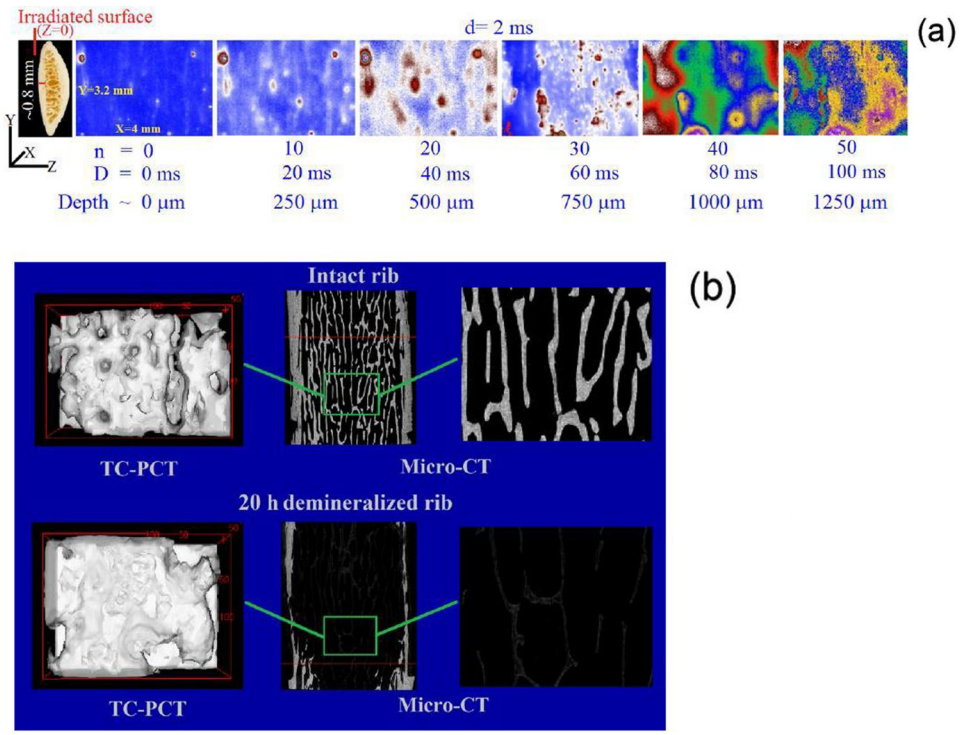

FIG. 10. Thermophotonic imaging of a bone sample. (a) Depth-coded planar images sampled at 20 ms reference-delay intervals, obtained from a goat rib. (b) Binarized amplitude TC-PCT and μCT images of the goat rib sample before and after demineralization. μCT images of the whole sample (~38-mm long) are shown in the central column. The region of interest for TC-PCT (4.0×3.2 mm^2) is delineated inside the center image. The TC-PCT image and zoomed-in version of the μCT image corresponding to the ROI are shown on the left and right columns, respectively. Unlike μCT, TC-PCT resolved both cortical and trabecular regions with high contrast for the post-demineralized sample.[71]

rate, and the maximum value is limited by the time difference between the last two pulses in the up-chirp waveform.

The amplitude peak value and the time corresponding to the peak value produce the amplitude and amplitude delay information, respectively. From the cross-correlation phase [Eq. (15)], the phase value at the amplitude peak time provides the phase of one pixel. From the resulting cross-correlation phase, the time corresponding to zero phase value provides the phase delay data of one pixel and specifies the net thermal flux of zero. For all pixels of the captured photothermal images, the truncation process provides tomographic slice TC-PCT amplitude, amplitude peak delay time, phase, and zero-delay phase planar images (tomograms) of an optically excited solid. Consequently, TC-PCT analysis provides four output channels: amplitude, peak delay time, phase, and zero-delay phase. By stacking depth-scaled planar images generated through phase incrementing the reference, TC-PCT can create three dimensional visualizations of the distribution of the object's photothermal parameters similar to OCT.

IV. THERMAL-WAVE IMAGING APPLICATIONS

A. Condition monitoring of industrial materials and art objects—Non-destructive testing

The use of non-destructive techniques is essential in industries where the failure of a component would cause a significant hazard or economic loss. Thermography has found many applications for maintenance inspections of industrial components and structures. LIT, PPT, and TWR are utilized in imaging hidden structures and defect detection within a short time in various objects such as steel,[8,38,58] aluminum,[59] ceramics,[49,60] composites,[61] carbon fiber reinforced plastics (CFRP),[55,62] wood,[49] Nylon®,[63] and concrete structures.[64] These thermal imaging technologies can accurately determine cracks, holes, or defects in a piece of material, which is important information for quality control to prevent breakdowns. An example of defect detection in aluminum is shown in Fig. 9. Two flat concentric bottom holes are drilled in a thick aluminum plate, one at the center of the other [Fig. 9(b)], and then imaged. PPT signal processing using wavelet transformation was applied to reconstruct the image shown in Fig. 9(a).[51]

Active thermography was successfully applied to investigations of the structure of paintings, subsurface delamination, and the degree of adhesion between paint layers.[11,65–67] In the field of art analysis, TC-PCT was applied to image the defective regions in a marquetry sample and successfully revealed holes, wood knots, glue rich areas, wood grain of the supporting layer of the marquetry, and delaminations.[68]

B. Medical applications—Biothermophotonics

Biomedical photothermics ("biothermophotonics") is an emerging non-ionizing, non-invasive diagnostic methodology based on spectrally selective optical absorption of modulated (or pulsed) electromagnetic radiation, thermal (non-radiative) conversion, and generation of thermal waves in tissues. Medical applications of thermophotonics are steadily growing since the sensitivity and specificity of these methods are inherently high.[69,70] Reports show the applicability of thermography techniques to biological tissues. However, the constraints imposed by the laser safety ceiling and the strong attenuation of thermal wave signals in tissues limit the detection depth in turbid media and tissues.[28,29] For example, in PPTR, where a single pulse excitation is used and raw data are not processed, subsurface absorber detection in turbid media and tissues is limited to ~1 mm.[30,31] The main concern with applying thermography techniques to biological tissues lies in its limitations to resolve deep lying absorbers over a depth of a few

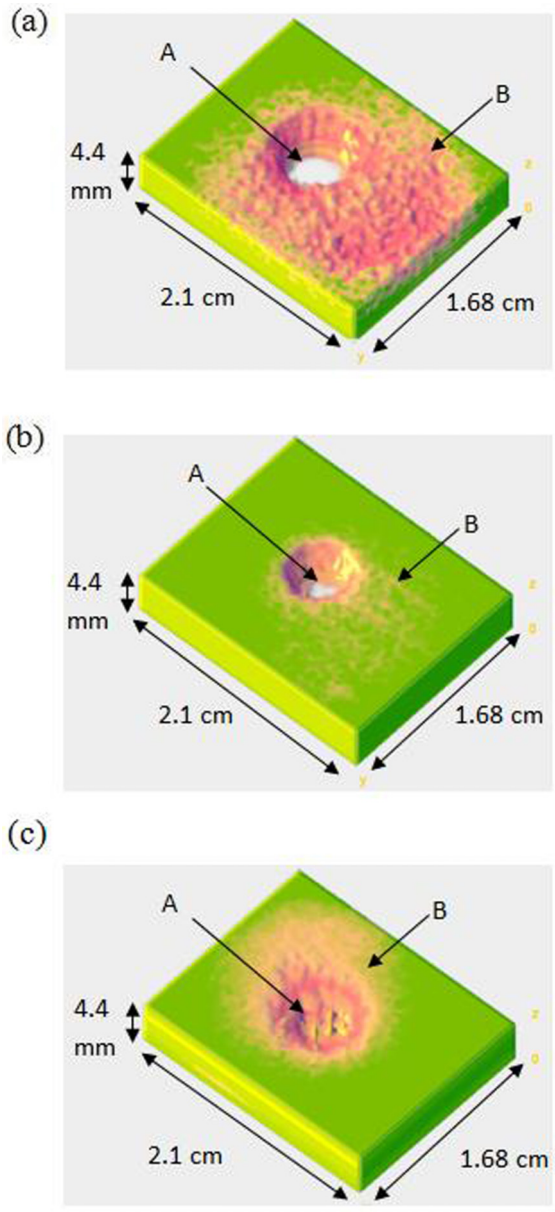

FIG. 11. Three-dimensional non-destructive enhanced TC-PCT imaging.[26] Amplitude tomograms of the enhanced TC-PCT of holes at the depth of 0.4 mm (a), 0.6 mm (b), and 1 mm (c) with truncation time gate of 40 ms. Each image covers an area of 2.1 cm × 1.68 cm on the sample, and the image delay time range is 1.2 s which corresponds to the depth of 4.39 mm. The $z = 0$ plane at the bottom of the image is the coordinate at which the camera recorded the thermal signals. A and B on these images display the holes, and the energy accumulation at the back surface, respectively. The images on (a)–(c) are not on the same scale. The laser beam illuminating the sample from the bottom is a pulsed chirped signal with a sweep range of 0.2 Hz-0.6 Hz, duration 12 s, and pulse duration 10 ms. Diameter of the illumination beam is 3 cm, and the laser intensity for the whole duration is 7 mJ/cm^2.[26]

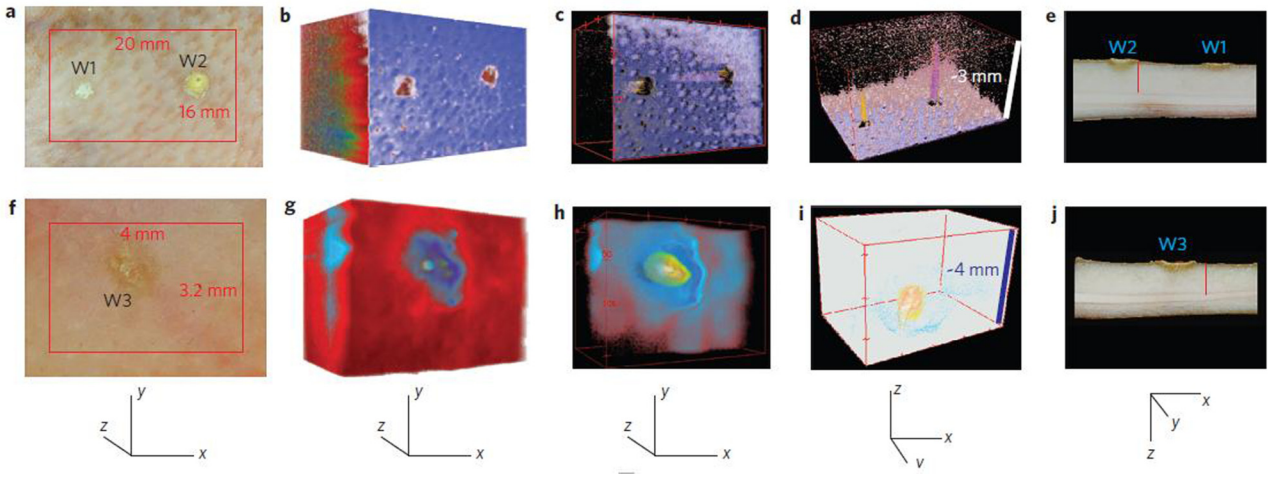

FIG. 12. Three-dimensional biothermophotonic application of TC-PCT to burn-depth analysis. In all images, the z axis (depth) is not shown on the actual scale but has been expanded for clarity. (a) Photograph of a pig's ear specimen with two burns. The red outline defines the imaged area. (b) Amplitude tomogram as observed from the tissue surface. (c) Amplitude tomogram with 60% transparency. The three-dimensional spatial distribution of burn injuries within the tissue can be observed. (d) Amplitude tomogram with transparency and threshold optimized for burn depth profile inspection. The needle-like structures at the bottom (x–y) are due to the follicles without hair whose presence can be seen in (a). (e) Photograph of the burn cross-section. Red scale bar, ~5 mm. Burn injuries extending down to a depth of ~2.5 mm can be observed. W2 is a severe burn, deeper and broader than W1. The extent of alteration of tissue parameters for W2 is higher than W1. (f) Photograph of the second sample with burn W3. (g) Amplitude tomogram as observed from the tissue surface. (h) Amplitude tomogram with 60% transparency. (i) Amplitude tomogram with transparency and threshold optimized for burn inspection. (j) Photograph of the burn cross-section. Red scale bar ~4 mm.[40]

millimeters while being maximum-permissible exposure (MPE) compatible.[17]

The first attempt in characterizing cortical bone with the aim of establishing a thermal imaging technology for the early diagnosis of osteoporosis was the development of CPPTR.[17] Skin and tissue overlayers strongly attenuate thermal waves generated in bones as a result of weak conductive thermal coupling between the bone and the skin surface. Additionally, re-absorption of emitted IR-photons by water molecules in the overlying tissues may occur, which forbids radiative coupling. CPPTR with superior SNR and depth profiling capability over the harmonically modulated TWR[38] and PPTR[28,30,31] was applied to monitor the degree of demineralization in a goat rib bone with overlayers of fat and skin. The largest bone thickness resolvable using CPPTR was ~1.8 mm with a fat-skin overlayer of ~1 mm thickness.[17] Later, TC-PCT was applied to imaging the structure of bones [Fig. 10].[71,72] TC-PCT demineralization tracking has been carried out to a depth of ~3.6 mm below the irradiated surface. Since the skin overlayer of a typical human wrist is in the range of 0.8–2 mm,[73,74] it is feasible to apply TC-PCT or even CPPTR to the diagnosis of human bone density for inspection of the wrist.

TC-PCT use has grown in a variety of applications from imaging subsurface defects and discontinuities in solids[26] and defectoscopy in art objects[68] to medical applications such as imaging burn depth profiles in tissues.[40] For NDI applications, TC-PCT provided defect detection in a steel sample at the depth of 4 mm, while lock-in thermography and the TWR reported maximum depth probing of 1.5 mm in the steel sample for the same imaging parameters.[26] A few examples of TC-PCT images of bone, holes in a steel sample, and burn depth profiles are presented in Figs. 10–12, respectively. Figure 10(a) shows TC-PCT amplitude planar images of a goat rib sampled at 20 ms reference-delay intervals. Figure 10(b) displays binarized amplitude TC-PCT compared with micro-computed tomography (μCT) images of the goat rib sample before and after demineralization. Figure 11 displays three holes at different depths in a steel sample. Application of TC-PCT to depth analysis of three burns in a pig's ear is shown in Fig. 12.

TC-PCT is the thermophotonic analog of OCT with better penetration depth in tissues (~3.6 mm in bones and more than 3.8 mm in teeth).[76] Although OCT offers high resolution images, its probe range is limited to less than 1 mm in bones, because of the highly scattering nature of light in hard tissues.[76,77] In contrast to photoacoustic imaging, which combines optical excitation and ultrasound detection, TC-PCT offers higher resolution, particularly in hard tissues. Photoacoustic imaging performs poorly with bone tissues due to severe attenuation of optical and ultrasound signals within bone structures, especially at higher frequencies that are necessary for enhanced resolution.[78] Axial resolution of photoacoustic imaging in bone diagnostics is in the range of 1 mm, while axial resolution of TC-PCT in bone imaging was measured to be ~25 μm.[40]

V. CONCLUSIONS AND OUTLOOK

With rapid improvements in the quality of infrared cameras over recent years, thermal imaging is attracting growing attention in biomedical applications and in the field of NDI of industrial materials and art analysis. In thermal wave imaging, energy conversion occurs between optical and thermal modes. Therefore, the specificity of the technique is inherently high because of its optical contrast, and its sensitivity is also high due to the energy conversion suppression of signal baselines which impart it with higher dynamic range than purely optical imaging modalities. Furthermore,

thermal-wave detection is very suitable for imaging turbid media such as biological tissues because it is not subject to resolution and depth-limiting optical and/or ultrasound scattering mechanisms.

Used for characterizing bone structures,[72] diagnosing dental caries,[39,75] visualizing burn depth profiles in tissue,[80] NDI applications to industrial materials, and in defectoscopy of art objects,[9,68] photothermal imaging (which also includes conventional thermography) has been proven to be a safe, reliable, sensitive, non-destructive, and non-contacting method for defect detection and structure studies. Thermal-wave analysis requires a modest amount of harmless optical radiation deposited onto a sample and is safer than X-rays. Therefore, we can reasonably expect rapid growth in the number of applications in wide ranges of fields from biomedical, industrial, dental, to artwork NDI.

ACKNOWLEDGMENTS

The authors gratefully acknowledge the Natural Sciences and Engineering Research Council (NSERC) Discovery Grants Program, the Canada Research Chairs Program, a CIHR-NSERC CHRP Grant to A. Mandelis for TC-PCT dental imaging applications, and the NSERC—Collaborative Research and Training Experience (CREATE) for financial support.

NOMENCLATURE

BPC	Binary phase coding
CFRP	Carbon fiber reinforced plastic
CPPTR	Chirped pulse photothermal radiometry
CW	Continuous wave
DFT	Discrete Fourier transform
EX-OR	Exclusive-OR
FFT	Fast Fourier Transform
HT	Hilbert Transform
IFFT	Inverse FFT
IR	Infrared
LFM	Linear frequency modulation
LIT	Lock-in thermography
MPE	Maximum-permissible exposure
NDI	Non-destructive imaging
OCT	Optical coherence tomography
PPT	Pulse phase thermography
PPTR	Pulse photothermal radiometry
PRBS	Pseudorandom binary sequence
PT	Pulsed Thermography
SNR	Signal-to-noise ratio
TCT	Thermal coherence tomography
TWR	Thermal wave radar
TC-PCT	Truncated-correlation photothermal coherence tomography
μ-CT	Micro-computed tomography

[1]J. A. Siddiqui, V. Arora, R. Mulaveesala, and A. Muniyappa, "Infrared thermal wave imaging for nondestructive testing of fibre reinforced polymers," Exp. Mech. **55**(7), 1239–1245 (2015).
[2]S. Ranjit, K. Kang, and W. Kim, "Investigation of lock-in infrared thermography for evaluation of subsurface defects size and depth," Int. J. Precis. Eng. Manuf. **16**(11), 2255–2264 (2015).
[3]S. Ranjit, M. Choi, and W. Kim, "Quantification of defects depth in glass fiber reinforced plastic plate by infrared lock-in thermography," J. Mech. Sci. Technol. **30**(3), 1111–1118 (2016).
[4]J. Yang, S. Hwang, Y. K. An, K. Lee, and H. Sohn, "Multi-spot laser lock-in thermography for real-time imaging of cracks in semiconductor chips during a manufacturing process," J. Mater. Process. Technol. **229**, 94–101 (2016).
[5]S. S. Pawar and V. P. Vavilov, "Applying the heat conduction-based 3D normalization and thermal tomography to pulsed infrared thermography for defect characterization in composite materials," Int. J. Heat Mass Transf. **94**, 56–65 (2016).
[6]R. Velazquez-Hernandez, A. Melnikov, A. Mandelis, K. Sivagurunathan, M. E. Rodriguez-Garcia, and J. Garcia, "Non-destructive measurements of large case depths in hardened steels using the thermal-wave radar," NDT E Int. **45**(1), 16–21 (2012).
[7]X. Guo, K. Sivagurunathan, J. Garcia, A. Mandelis, S. Giunta, and S. Milletari, "Laser photothermal radiometric instrumentation for fast in-line industrial steel hardness inspection and case depth measurements," Appl. Opt. **48**(7), C11–C23 (2009).
[8]J. Y. Liu, J. L. Gong, and L. Qin, "Three-dimensional visualization of subsurface defect using lock-in thermography," Int. J. Thermophys. **36**(5–6), 1226–1235 (2015).
[9]D. Gavrilov, R. G. Maev, and D. P. Almond, "A review of imaging methods in analysis of works of art: Thermographic imaging method in art analysis," Can. J. Phys. **92**(4), 341–364 (2014).
[10]S. Sfarra, C. Ibarra-Castanedo, D. Ambrosini, D. Paoletti, A. Bendada, and X. Maldague, "Integrated approach between pulsed thermography, near-infrared reflectography and sandwich holography for wooden panel paintings advanced monitoring," Russ. J. Nondestr. Test. **47**(4), 284–293 (2011).
[11]B. F. Miller, "The feasibility of using thermography to detect subsurface voids in painted wooden panels," J. Am. Inst. Conserv. **16**(2), 27–35 (1977).
[12]A. Kirsh and R. S. Levenson, *Seeing Through Paintings: Physical Examination in Art Historical Studies* (Yale University Press, 2002).
[13]N. Tabatabaei, A. Mandelis, and B. T. Amaechi, "Thermophotonic lock-in imaging of early demineralized and carious lesions in human teeth," J. Biomed. Opt. **16**(7), 071402 (2011).
[14]J. Jan, W. Z. Wan Bakar, S. M. Mathews, L. O. Okoye, B. R. Ehler, C. Louden, and B. T. Amaechi, "Proximal caries lesion detection using the Canary Caries Detection System: An in vitro study," J. Investig. Clin. Dent. **7**(4), 383–390 (2016).
[15]J. D. Silvertown, B. Y. Wong, K. Sivagurunathan, S. H. Abrams, J. Kirkham, and B. T. Amaechi, "Remineralization of natural early caries lesions in vitro by P11–4 monitored with photothermal radiometry and luminescence," J. Investig. Clin. Dent. **8**(4), 12257 (2017).
[16]J. D. Silvertown, B. Y. Wong, S. H. Abrams, K. Sivagurunathan, S. M. Mathews, and B. T. Amaechi, "Comparison of The Canary System and DIAGNOdent for the in vitro detection of caries under opaque dental sealants," J. Investig. Clin. Dent. **8**(4), 12239 (2016).
[17]S. Kaiplavil and A. Mandelis, "Highly depth-resolved chirped pulse photothermal radar for bone diagnostics," Rev. Sci. Instrum. **82**, 074906 (2011).
[18]S. Kaiplavil and A. Mandelis, "Ultra-deep bone diagnostics with fat–skin overlayers using new pulsed photothermal radar," Int. J. Thermophys. **34**, 1481–1488 (2013).
[19]M. Gautherie and C. M. Gros, "Breast thermography and cancer risk prediction," Cancer **45**(1), 51–56 (1980).
[20]J. Koay, C. Herry, and M. Frize, "Analysis of breast thermography with an artificial neural network," Conf. Proc. IEEE Eng. Med. Biol. Soc. **2**, 1159–1162 (2004).
[21]S. Ciatto, M. Rosselli Del Turco, S. Cecchini, G. Grazzini, and A. Lossa, "Telethermography and breast cancer risk prediction," Tumori **75**(2), 110–112 (1989).
[22]A. Lashkari, F. Pak, and M. Firouzmand, "Full intelligent cancer classification of thermal breast images to assist physician in clinical diagnostic applications," J. Med. Signals Sens. **6**(1), 12–24 (2016).
[23]A. Mandelis, "Diffusion waves and their uses," Phys. Today **53**(8), 29–34 (2000).
[24]V. P. Vavilov and S. Marinetti, "Pulse phase thermography and thermal tomography using Fourier transformation," Russ. J. Nondestruct. Test. **35**(2), 58–72 (1999).

[25]G. Busse, "Optoacoustic phase angle measurement for probing a metal," Appl. Phys. Lett. **35**(10), 759–760 (1979).
[26]P. Tavakolian, K. Sivagurunathan, and A. Mandelis, "Enhanced truncated-correlation photothermal coherence tomography with application to deep subsurface defect imaging and 3-dimensional reconstructions," J. Appl. Phys. **122**, 023103 (2017).
[27]G. Busse, D. Wu, and W. Karpen, "Thermal wave imaging with phase sensitive modulated thermography," J. Appl. Phys. **71**, 3962–3965 (1992).
[28]S. A. Prahl, I. A. Vitkin, U. Bruggemann, B. C. Wilson, and R. R. Anderson, "Determination of optical properties of turbid media using pulsed photothermal radiometry," Phys. Med. Biol. **37**, 1203–1217 (1992).
[29]A. Mandelis and P. Hess, *Progress in Photothermal and Photoacoustic Science and Technology: Life and Earth Sciences* (SPIE Press, Bellingham, WA, 1997), Chap 11, p. 454.
[30]A. C. Tam, "Pulsed photothermal radiometry for noncontact spectroscopy, material testing and inspection measurements," Infrared Phys. **25**, 305–313 (1985).
[31]W. P. Leung and A. C. Tam, "Techniques of flash radiometry," J. Appl. Phys. **56**, 153–161 (1984).
[32]X. Maldague and S. Marinetti, "Pulse phase infrared thermography," J. Appl. Phys. **79**(5), 2694 (1996).
[33]G. F. Kirkbright and R. M. Miller, "Cross-correlation techniques for signal recovery in thermal wave imaging," Anal. Chem. **55**(3), 502–506 (1983).
[34]A. Mandelis, "Frequency modulated (FM) time delay photoacoustic and photothermal wave spectroscopies. Technique, instrumentation, and detection. Part I: Theoretical," Rev. Sci. Instrum. **57**(4), 617–621 (1986).
[35]A. Mandelis, L. M. L. Borm, and J. Tiessinga, "Frequency modulated (FM) time delay photoacoustic and photothermal wave spectroscopies. Technique, instrumentation, and detection. Part II: Mirage effect spectrometer design and performance," Rev. Sci. Instrum. **57**(4), 622–629 (1986).
[36]A. Mandelis, L. M. L. Borm, and J. Tiessinga, "Frequency modulated (FM) time delay photoacoustic and photothermal wave spectroscopies. Technique, instrumentation, and detection. Part III: Mirage effect spectrometer, dynamic range, and comparison to pseudo-random-binary-sequence (PRBS) method," Rev. Sci. Instrum. **57**(4), 630–635 (1986).
[37]R. Mulaveesala, J. S. Vaddi, and P. Singh, "Pulse compression approach to infrared nondestructive characterization," Rev. Sci. Instrum. **79**(9), 094901 (2008).
[38]N. Tabatabaei and A. Mandelis, "Thermal-wave radar: A novel subsurface imaging modality with extended depth-resolution dynamic range," Rev. Sci. Instrum. **80**(3), 034902 (2009).
[39]N. Tabatabaei and A. Mandelis, "Thermal coherence tomography using match filter binary phase coded diffusion waves," Phys. Rev. Lett. **107**, 165901 (2011).
[40]S. Kaiplavil and A. Mandelis, "Truncated-correlation photothermal coherence tomography for deep subsurface analysis," Nat. Photonics **8**(8), 635–642 (2014).
[41]X. Maldague, *Theory and Practice of Infrared Technology for Nondestructive Testing* (John Wiley Interscience, New York, 2001), p. 704.
[42]G. Busse, "Photothermal transmission probing of a metal," Infrared Phys. **20**(6), 419 (1980).
[43]G. Busse and P. Eyerer, "Thermal wave remote and nondestructive inspection of polymers," Appl. Phys. Lett. **43**(4), 355 (1983).
[44]P. E. Nordal and S. O. Kanstad, "Visible-light spectroscopy by photothermal radiometry using an incoherent source," Appl. Phys. Lett. **38**(7), 486 (1981).
[45]A. Mandelis, *Diffusion-Wave Fields: Mathematical Methods and Green Functions* (Springer Science, New York, 2001), p. 741.
[46]K. D. Cole, J. V. Beck, A. Haji-Sheikh, and B. Litkouhi, *Heat Conduction Using Green's Functions* (Taylor & Francis Group CRC press, 2010), p. 663.
[47]R. Tai, J. Zhang, C. Wang, and A. Mandelis, "Thermal-wave fields in solid wedges using the Green function method: Theory and experiment," J. Appl. Phys. **113**, 133501 (2013).
[48]C. Wang, A. Mandelis, and Y. Liu, "Photothermal radiometry with solid cylindrical samples," J. Appl. Phys. **96**, 3756 (2004).
[49]D. T. Wu and G. Busse, "Lock-in thermography for nondestructive evaluation of materials," Rev. Gén. Therm. **37**(8), 693–703 (1998).
[50]A. Mandelis, S. Paoloni, and L. Nicolaides, "Novel lock-in waveform technique for signal-to-noise ratio and dynamic range enhancement in highly noised photothermal experiments," Anal Sci. **17**, s5–s8 (2001).
[51]X. Maldague, F. Galmiche, and A. Ziadi, "Advances in pulsed phase thermography," Infrared Phys. Technol. **43**(3–5), 175–181 (2002).
[52]C. Ibarra-Castanedo and X. Maldague, "Pulsed phase thermography reviewed," QIRT J. **1**(1), 47–70 (2004).
[53]C. Ibarra-Castanedo and X. Maldague, "Review of pulsed phase thermography," Proc. SPIE **9485**, 94850T (2015).
[54]F. Galmiche and X. Maldague, "Depth defect retrieval using the wavelet pulsed phased thermography," *Proceedings of the 5th Conference on Quantitative Infrared Thermography (QIRT)*, Seminar 64 (2000), pp. 194–199.
[55]R. Mulaveesala and S. Tuli, "Theory of frequency modulated thermal wave imaging for nondestructive subsurface defect detection," Appl. Phys. Lett. **89**(19), 191913 (2006).
[56]N. Levanon and E. Mozeson, *Radar Signals* (Wiley, 2004).
[57]N. Tabatabaei, "Matched-filter thermography," Appl. Sci. **8**(4), 581 (2018).
[58]S. Delanthabettu, M. Menaka, B. Venkatraman, and B. Raj, "Defect depth quantification using lock-in thermography," Quant. Infrared Thermogr. J. **12**(1), 37–52 (2015).
[59]J. Couturier and X. Maldague, "Pulsed phase thermography of aluminum specimens," Proc. SPIE **3056**, 170–175 (1997).
[60]N. Simões, I. Simões, A. Tadeu, and C. Serra, "Evaluation of adhesive bonding of ceramic tiles using active thermography," QIRT Conference Paper (2012).
[61]W. Bai and B. S. Wong, "Evaluation of defects in composite plates under convective environments using lock-in thermography," Meas. Sci. Technol. **12**, 142–150 (2001).
[62]C. Meola, "Nondestructive evaluation of materials with rear heating lock-in thermography," IEEE Sens. J. **7**(10), 1388–1389 (2007).
[63]S. Marinetti, Y. A. Plotnikov, W. P. Winfree, and A. Braggiotti, "Pulse phase thermography for defect detection and visualization," Proc. SPIE **3586**, 10 (1999).
[64]T. Sakagami and S. Kubo, "Development of a new non-destructive testing technique for quantitative evaluations of delamination defects in concrete structures based on phase delay measurement using lock-in thermography," Infrared Phys. Technol. **43**(3–5), 311–316 (2002).
[65]N. P. Avdelidis, M. Koui, C. Ibarra-Castanedo, and X. Maldague, "Thermographic studies of plastered mosaics," Infrared Phys. Technol. **49**(3), 254–256 (2006).
[66]K. Blessley, C. Young, J. Nunn, J. Coddington, and S. and Shepard, "The feasibility of flash thermography for the examination and conservation of works of art," Stud. Conserv. **55**(2), 107 (2010).
[67]S. Sfarra, P. Theodorakeas, J. Cernecký, E. Pivarciová, S. Perilli, and M. and Koui, "Inspecting marquetries at different wavelengths: The preliminary numerical approach as aid for a wide-range of non-destructive tests," J. Nondestr. Eval. **36**(1), 6 (2017).
[68]P. Tavakolian, S. Sfarra, G. Gargiulo, K. Sivagurunathan, and A. Mandelis, "Photothermal coherence tomography for 3-D visualization and structural non-destructive imaging of a wood inlay," Infrared Phys. **91**, 206–213 (2018).
[69]L. V. Wang and H. Wu, *Biomedical Optics Principles and Imaging* (Wiley, 2007), p. 376.
[70]N. A. Diakides, "The growing applications of medical infrared imaging," IEEE Eng. Med. Biol. Mag. **19**(3), 28–29 (2000).
[71]S. Kaiplavil, A. Mandelis, and B. T. Amaechi, "Truncated-correlation photothermal coherence tomography of artificially demineralized animal bones: Two- and three-dimensional markers for mineral loss monitoring," J. Biomed. Opt. **19**(2), 026015 (2014).
[72]S. Kaiplavil, A. Mandelis, X. Wang, and T. Feng, "Photothermal tomography for the functional and structural evaluation, and early mineral loss monitoring in bones," Biomed. Opt. Express **5**(8), 2488–2502 (2014).
[73]B. D. Fornage and J. L. Deshayes, "Ultrasound of normal skin," J. Clin. Ultrasound **14**(8), 619–622 (1986).
[74]H. Alexander and D. L. Miller, "Determining skin thickness with pulsed ultra sound," J. Invest. Dermatol. **72**(1), 17–19 (1979).
[75]M. Razani, K. Sivagurunathan, P. Tavakolian, S. Roointan, E. B. Shokouhia, N. Tabatabaei, and A. Mandelis, "Photothermal coherence tomography for 3D visualization of dental caries," Proc. SPIE, 10473–10472 (2018).
[76]C. Kasseck, M. Kratz, A. Torcasio, N. C. Gerhardt, G. H. van Lenthe, T. Gambichler, K. Hoffmann, D. B. Jones, and M. R. Hofmann, "Comparison of optical coherence tomography, microcomputed tomography, and histology at a three-dimensionally imaged trabecular bone sample," J. Biomed. Opt. **15**(4), 046019 (2010).

[77]W. Drexler, "Ultrahigh-resolution optical coherence tomography," J. Biomed. Opt. **9**, 47–74 (2004).
[78]X. Wang, D. L. Chamberland, P. L. Carson, J. B. Fowlkes, R. O. Bude, D. A. Jamadar, and B. J. Roessler, "Imaging of joints with laser-based photoacoustic tomography: An animal study," Med. Phys. **33**(8), 2691–2697 (2006).
[79]Roointan, S., Tavakolian, P., K. Sivagurunathan, M. Floryan, A. Mandelis, and S. H. Abrams, "3D subsurface imaging of healthy and carious human teeth using enhanced truncated-correlation photothermal coherence tomography," Nat. Biomed. Eng. (submitted).
[80]H. E. John, V. Niumsawatt, W. M. Rozen, and I. S. Whitaker, "Clinical applications of dynamic infrared thermography in plastic surgery: A systematic review," Gland Surg. **5**(2), 122–132 (2016).
[81]N. Tabatabaei and A. Mandelis, "Thermal wave radar," J. Phys. Conf. Ser. **214**, 012088 (2010).